Improving Positioning Accuracy of UWB in Complicated Underground NLOS Scenario Using Calibration, VBUKF, and WCA

Bo Cao, Shibo Wang, Shirong Ge, and Wanli Liu

***Abstract*— Accurate localization of the shearer is key to achieving efficient, automated, unmanned mining. Unfortunately, the existing positioning algorithms usually yields low-precision, insufficient applicability, and unreliable final estimation due to the existence of non-line-of-sight (NLOS) error and also because they ignore the position error of anchor nodes (ANs). To bridge this technology gap, we developed a novel localization strategy by incorporating calibration, variational Bayesian unscented Kalman filter (VBUKF), total least squares (TLS), and water cycle algorithm (WCA) to enhance the location estimation accuracy of ultrawideband (UWB) positioning system in a complicated underground environment. First, calibration was implemented based on the selection of appropriate reference nodes (RNs) in line-of-sight (LOS) scenarios to estimate the scale-factor error, bias, and position errors for each AN; then the VBUKF smoothing with the consideration of time-variant measurement noise was used to reduce the interference of NLOS owing to the difficult separation of bias and NLOS error. Second, the TLS method was implemented to calculate the target node's position based on the smoothed distances and calibrated positions of ANs. Lastly, the WCA embedded scheme was executed to further ameliorate estimation accuracy. The experimental results demonstrated that the proposed TLS-WCA approach, after the implementation of calibration and VBUKF, was best able to improve the localization accuracy remarkably, and outperformed the other compared methods, which can efficiently attain higher estimation accuracy, highlighting the outstanding localization performance.**

***Index Terms*— Positioning calibration, total least squares (TLS), underground environment, variational bayesian unscented Kalman filter (VBUKF), water cycle algorithm (WCA).**

Manuscript received October 25, 2020; accepted October 26, 2020. Date of publication November 3, 2020; date of current version January 5, 2021. This work was supported in part by the Joint Funds of the National Natural Science Foundation of China under Grant U1610251, Grant U51874279, and Grant 51974290, in part by the National Key Research and Development Program of China under Grant 2018YFC0604503, and in part by the Priority Academic Program Development (PAPD) of Jiangsu Higher Education Institutions. The Associate Editor coordinating the review process was Alessio De Angelis. *(Corresponding authors: Shibo Wang; Wanli Liu.)*

Bo Cao is with the College of Mechatronic Engineering, China University of Mining and Technology, Xuzhou 221116, China, and also with the School of Mechanic Engineering, Anhui Institute of Science and Technology, Bengbu 233100, China (e-mail: shanxi2008caobo@163.com).

Shibo Wang and Wanli Liu are with the College of Mechatronic Engineering, China University of Mining and Technology, Xuzhou 221116, China (e-mail: wangshb@cumt.edu.cn; 4830@cumt.edu.cn).

Shirong Ge is with the College of Mechatronic Engineering, China University of Mining and Technology, Beijing 100083, China (e-mail: gesr@cumt.edu.cn).

Digital Object Identifier 10.1109/TIM.2020.3035579

I. Introduction

UNMANNED and automated mining is a promising technology being pursued in the coal mining field at home and abroad to improve productivity and decrease injuries to human workers [1]. The shearer is a crucial component for a fully mechanized mining face (FMMF), the position and attitude of which determine the running state of hydraulic supports and scraper conveyor [2], [3]. Hence, accurately monitoring and acquiring the location of a shearer is of great importance if automated mining is to be perfected [4]. The presently available inertial navigation system (INS) has been widely applied to estimate the shearer's location in the coal mine environment, but the estimation accuracy of this method commonly degrades with time due to the typical drift of INS [1], [5]. Thus, it was indispensable to incorporate other positioning techniques to account for the error resulting from INS drift when the shearer reached the end of FMMF. One such positioning method is state-of-the-art ultrawideband (UWB) technique, which has shown considerable potential for ranging and localization due to the remarkable advantages of large bandwidth, high precision ranging, good antimultipath effect [6], high-speed wireless data transmission, and good obstacle-penetration capacity [7]. UWB has been broadly used in both military and civilian fields, giving it the additional advantage of having been applied in the underground environment.

Till now, several reports have described the use of the UWB system to improve underground localization. In these studies, the UWB positioning system was fused into the INS utilizing either loosely coupled [8], [9], or tightly coupled approaches [10]. Li *et al.* [11] proposed the use of a pseudo-GPS positioning system in the coal mine employing UWB range measurements utilizing the error state Kalman filter (KF) to fuse measurements from the INS and UWB system. Fan *et al.* [12] proposed a strategy that utilized the UWB positioning system to aid INS, in which the anchor nodes (ANs) were installed on the hydraulic supports, and a target node (TN) was mounted on the shearer. Wang *et al.* [13] developed a tightly coupled GPS/UWB/INS cooperative positioning algorithm based on a robust KF. Tian *et al.* [14] presented a UWB/INS integrated system using only one AN in an unknown position. However, the aforementioned localization schemes could only be effectively implemented in line-of-sight (LOS) scenario, these approaches were formidable to generate

reliable and satisfying location estimates in non-line-of-sight (NLOS) situation due to the existence of NLOS error, and this lower localization accuracy limited the applicability of these methods.

Generally, the underground mining space is a highly complex environment with high dust contents, moving targets, irregular objects, and the dynamically changing FMMF, and the UWB signal channel can be affected by those obstructions, resulting in NLOS error [15]. Numerous approaches have been proposed to eliminate NLOS error, which was categorized into two types: NLOS identification and NLOS mitigation. The NLOS error identification schemes commonly depended on channel impulse responses [16], [17], hypothesis testing [18], machine learning [19], [20], statistical analyses methods [21], and likelihood ratio tests [22]. For NLOS error mitigation, the chief techniques have focused on the residual weighted localization algorithm [23], Taylor series least squares (LS) method [24], constraint optimization [25], KF [26], extended KF (EKF) [27], H-infinity filter (HIF) [28], unscented KF (UKF) [29], and cubature KF (CKF) [30]. However, both the KF and HIF are suitable only for linear systems, not nonlinear systems [31], and while the EKF linearizes the nonlinear system model by calculating the Jacobian matrix [30], its performance can be severely degraded when the measurement system is highly nonlinear [32]. In contrast, the UKF avoids computing the cumbersome Jacobian matrices by providing derivative-free higher-order approximations which are more accurate performance than the EKF [33]. The performance of the UKF could achieve the precision of the third-degree UKF [34]. Nevertheless, these filters mentioned-above had limitations and were insufficiently effective to solve the filtering issues because they required definite statistics of noise [35], which was impractical to ascertain in real-world applications. This was because the UWB signal was susceptible to the external circumstances, and the measurement noise changed dynamically with the different positioning points. To avoid performance degradation, the variational Bayesian [36] (VB)-based filtering methods have been developed to deal with the unknown and time-variant measurement noise. The VB adaptive KF (VBAKF) scheme was put forward to approximate the time-variant measurement noise variances as well as the system state [37]. Moreover, Huang *et al.* [38] proposed a novel VBAKF, which exhibited good filtering performance and was more robust to the uncertainties of the process and measurement noise covariance. Huang *et al.* [39] used their novel VBAKF to approximate the time-variant measurement noise to account for the NLOS error, and the results showed that the measurement NLOS errors were notably reduced. Cao *et al.* [15] proposed two parallel VBAKFs using an interacting multiple model approach structure to mitigate the LOS and NLOS errors in mixed LOS/NLOS conditions. Consequently, inspired by the above-noted research and thanks to the VB's superior flexibility, in this article, we utilized the VB to approximate the changeable and unknown measurement noise and adopted the UKF to update the state to reduce the impact of NLOS error.

In real-world tests, it has generally been accepted that the position coordinates of ANs must be determined with the highest possible accuracy within the positioning space before the UWB experiments are conducted. However, in practice, the positioning error caused by inaccurate installation and the unavoidable measurement error of ANs' positions results in low positioning accuracy. The main factors affecting the positioning accuracy of the UWB system were usually channel error and NLOS error, in which the domain channel error was the scale-factor and bias errors. Many existing literature works have attempted to remove the bias error to enhance positioning performance [40]–[43]. Nevertheless, it was impossible to obtain the position of ANs with sufficient accuracy in practical applications, and the positioning accuracy was affected significantly by the position errors of ANs. The above-cited studies were assumed that the positions of all ANs were known accurately without considering the AN's position error, which resulted in poor localization accuracy. This motivated us to address the issue of AN position error for TN localization in unknown and uncertain environments. Thus, in this article, to enrich the positioning methodology and reduce the estimation inaccuracy introduced by the NLOS error and AN installation error, we proposed a novel positioning strategy that considered both the AN position error and the NLOS time-variant measurement noise. More specifically, we utilized the proposed approach to calculate the scale-factor error, bias, along with the AN installation position error, and then used these calculations to calibrate the positions of each AN. Subsequently, with the consideration of the time-variant measurement noise, the variational Bayesian unscented Kalman filter (VBUKF) was utilized to reduce the NLOS error in real-time and improve the quality of the measured distances. Finally, the total least squares (TLS) method was adopted to compute the position of the TN using the filtered distance of the VBUKF technique and the calibrated AN position coordinates, and the water cycle algorithm (WCA) was executed to further ameliorate the overall positioning accuracy. To certify the outstanding performance of the proposed TLS-WCA technique after calibration and VBUKF smoothing, we utilized the Gaussian–Newton algorithm (GNA) to optimize the TLS result and compared them with TLS and TLS-WCA method before and after AN position calibration and VBUKF smoothing. The chief contributions of this study can be summarized as follows.

1) A novel calibration strategy approach was proposed that accounted for both the installation location error of ANs and the scale-factor as well as bias error during localization in an underground mine environment.
2) VBUKF smoothing was introduced to diminish NLOS error and obtain a more accurate distance estimation between TN and the corresponding AN.
3) The WCA method was used to optimize the TLS result, and both the static and dynamic experiments in the evaluation scenario were, respectively, conducted to validate the superiority and adaptability of the proposed TLS-WCA technique. These comparative experimental results demonstrated the efficacy of the proposed strategy, and the positioning accuracy can be remarkably enhanced possessing higher robustness.

II. Calibration and VBUKF Smoothing

A. Calibration

Without loss of generality, the measured distance between TN and the ith AN donated by r_i is expressed as follows:

$$r_i = \sqrt{\left(x_i^{\mathrm{AN}} - x^{\mathrm{TN}}\right)^2 + \left(y_i^{\mathrm{AN}} - y^{\mathrm{TN}}\right)^2 + \left(z_i^{\mathrm{AN}} - z^{\mathrm{TN}}\right)^2} \quad (1)$$

where $(x_i^{\mathrm{AN}}, y_i^{\mathrm{AN}}, z_i^{\mathrm{AN}})$ and $(x_i^{\mathrm{TN}}, y_i^{\mathrm{TN}}, z_i^{\mathrm{TN}})$, respectively, indicate the coordinates of the ith AN and TN.

The measurement distance d_i was larger than the real distance because the UWB signal was affected by the error in the ranging system and NLOS error, given by

$$d_i = (1+\alpha_i) r_i + B_i + N_i + w_i \quad (2)$$

where α_i indicates the scale-factor error; B_i indicates the bias; N_i indicates the NLOS error; w_i indicates white Gaussian noise.

The scale-factor α_i and bias errors B_i can be compensated by utilizing an appropriate calibration technique. If the UWB positioning system was in an LOS scenario, the parameter α_i and B_i would be computed and the position of the ANs could be calibrated. In this circumstance, it was assumed that the exact position coordinates of the ANs have been acquired. However, as discussed above, in complex scenarios such as the underground environment, determining the exact coordinates of the ANs was impractical due to the errors inherent in the processes of installation and measurement of AN locations. Thus, (2) must be transformed into the following form:

$$d_i = (1+\alpha_i)\sqrt{\left(x_i^{\mathrm{TN}}\right)^2 + \left(y_i^{\mathrm{TN}}\right)^2 + \left(z_i^{\mathrm{TN}}\right)^2} + B_i + N_i + w_i \quad (3)$$

where $x_i^{\mathrm{TN}} = \hat{x}_i^{\mathrm{AN}} - \delta x_i^{\mathrm{AN}} - x^{\mathrm{TN}}$, $y_i^{\mathrm{TN}} = \hat{y}_i^{\mathrm{AN}} - \delta y_i^{\mathrm{AN}} - y^{\mathrm{TN}}$, $z_i^{\mathrm{TN}} = \hat{z}_i^{\mathrm{AN}} - \delta z_i^{\mathrm{AN}} - z^{\mathrm{TN}}$; $(\delta x_i^{\mathrm{AN}}, \delta y_i^{\mathrm{AN}}, \delta z_i^{\mathrm{AN}})$ represents the position error of the ith AN; and $(\hat{x}_i^{\mathrm{AN}}, \hat{y}_i^{\mathrm{AN}}, \hat{z}_i^{\mathrm{AN}})$ indicates the erroneous position coordinates.

To better implement the calibration of ANs positions, the NLOS error can be ignored and multiple appropriate reference nodes (RNs) should be selected in LOS scenarios; that was, the LOS measurement distance can then be collected in such condition. Additionally, note that the RNs position coordinates were measured as accurately as possible. By using the UWB positioning system, the measurement distances d_{i-j} between the ith AN and the jth RN can be formulated as follows:

$$d_{i-j} = (1+\alpha_i)\sqrt{\left(x_{i-j}^{\mathrm{RN}}\right)^2 + \left(y_{i-j}^{\mathrm{RN}}\right)^2 + \left(z_{i-j}^{\mathrm{RN}}\right)^2} + B_i + w_{i-j} \quad (4)$$

where $x_{i-j}^{\mathrm{RN}} = \hat{x}_i^{\mathrm{AN}} - \delta x_i^{\mathrm{AN}} - x_j^{\mathrm{RN}}$, $y_{i-j}^{\mathrm{RN}} = \hat{y}_i^{\mathrm{AN}} - \delta y_i^{\mathrm{AN}} - y_j^{\mathrm{RN}}$, $z_{i-j}^{\mathrm{RN}} = \hat{z}_i^{\mathrm{AN}} - \delta z_i^{\mathrm{AN}} - z_j^{\mathrm{RN}}$; $(x_j^{\mathrm{RN}}, y_j^{\mathrm{RN}}, z_j^{\mathrm{RN}})$ indicates the position coordinates of the jth RN.

As can be seen in (4), scale-factor error, bias, and position error are intertwined with each other, which is not conducive to obtaining the three error parameters independently. Hence, in this article, we have proposed a calibration technique to estimate the aforementioned parameters effectively. First, the bias can be considered as a fixed value for each AN in an LOS situation, and thus the bias can be eliminated by calculating the differences between various measurements for the same AN. Subsequently, the scale-factor error and position error can be computed by linearizing the equation.

To implement the calibration efficiently, we first choose one common RN from the n RNs, and the remaining $n-1$ ranging equations are subtracted from the common raging equation, respectively, expressed as follows:

$$\begin{aligned} d_{i-j} - d_{i-C} = {} & (1+\alpha_i)\sqrt{\left(x_{i-j}^{\mathrm{RN}}\right)^2 + \left(y_{i-j}^{\mathrm{RN}}\right)^2 + \left(z_{i-j}^{\mathrm{RN}}\right)^2} \\ & - (1+\alpha_i)\sqrt{\left(x_{i-C}^{\mathrm{RN}}\right)^2 + \left(y_{i-C}^{\mathrm{RN}}\right)^2 + \left(z_{i-C}^{\mathrm{RN}}\right)^2} + w_i \end{aligned} \quad (5)$$

where $i = 1, 2, \ldots, n-1$; and C represents the common RN.

By substituting (4) into (5) and performing Taylor series first-order expansion at the point $(\hat{x}_i^{\mathrm{AN}}, \hat{y}_i^{\mathrm{AN}}, \hat{z}_i^{\mathrm{AN}})$ yields the following form:

$$\begin{aligned} & \left(d_{i-j} - d_{i-C}\right) - \left(\hat{d}_{i-j} - \hat{d}_{i-c}\right) \\ & = -M_{i-j}^x \delta x_i^{\mathrm{AN}} - M_{i-j}^y \delta y_i^{\mathrm{AN}} - M_{i-j}^z \delta z_i^{\mathrm{AN}} + \left(\hat{d}_{i-j} - \hat{d}_{i-c}\right)\alpha_i + w_i \end{aligned} \quad (6)$$

where the detailed derivation of Taylor expansion is expressed in Appendix B

$$\begin{aligned} \hat{d}_{i-j} &= \sqrt{\left(\hat{x}_i^{\mathrm{AN}} - x_j^{\mathrm{RN}}\right)^2 + \left(\hat{y}_i^{\mathrm{AN}} - y_j^{\mathrm{RN}}\right)^2 + \left(\hat{z}_i^{\mathrm{AN}} - z_j^{\mathrm{RN}}\right)^2} \\ M_{i-j}^x &= \left(\frac{\hat{x}_i^{\mathrm{AN}} - x_j^{\mathrm{RN}}}{\hat{d}_{i-j}} - \frac{\hat{x}_i^{\mathrm{AN}} - x_c^{\mathrm{RN}}}{\hat{d}_{i-c}}\right) \\ M_{i-j}^y &= \left(\frac{\hat{y}_i^{\mathrm{AN}} - y_j^{\mathrm{RN}}}{\hat{d}_{i-j}} - \frac{\hat{y}_i^{\mathrm{AN}} - y_c^{\mathrm{RN}}}{\hat{d}_{i-c}}\right) \\ M_{i-j}^y &= \left(\frac{\hat{y}_i^{\mathrm{AN}} - y_j^{\mathrm{RN}}}{\hat{d}_{i-j}} - \frac{\hat{y}_i^{\mathrm{AN}} - y_c^{\mathrm{RN}}}{\hat{d}_{i-c}}\right). \end{aligned}$$

Equation (6) can be converted into the matrix form

$$U_i = G_i X_i + W \quad (7)$$

where

$$U_i = \begin{bmatrix} \left(d_{i-1} - d_{i-C}\right) - \left(\hat{d}_{i-1} - \hat{d}_{i-c}\right) \\ \left(d_{i-2} - d_{i-C}\right) - \left(\hat{d}_{i-2} - \hat{d}_{i-c}\right) \\ \vdots \\ \left(d_{i-(n-1)} - d_{i-C}\right) - \left(\hat{d}_{i-(n-1)} - \hat{d}_{i-c}\right) \end{bmatrix}$$

$$X_i = \begin{bmatrix} \delta x_i^{\mathrm{AN}} \\ \delta y_i^{\mathrm{AN}} \\ \delta z_i^{\mathrm{AN}} \\ \alpha_i \end{bmatrix}$$

$$G_i = \begin{bmatrix} -M_{i-1}^x & -M_{i-1}^y & -M_{i-1}^z & \hat{d}_{i-1} - \hat{d}_{i-c} \\ -M_{i-2}^x & -M_{i-2}^y & -M_{i-2}^z \hat{d}_{i-2} & -\hat{d}_{i-c} \\ \vdots & \vdots & \vdots & \vdots \\ -M_{i-(n-1)}^x & -M_{i-(n-1)}^y & -M_{i-(n-1)}^z & \hat{d}_{i-(n-1)} - \hat{d}_{i-c} \end{bmatrix}.$$

By utilizing the LS approach, the scale-factor error and position error of the ith AN can be calculated as follows:

$$\begin{bmatrix} \delta \tilde{x}_i^{\mathrm{AN}} \\ \delta \tilde{y}_i^{\mathrm{AN}} \\ \delta \tilde{z}_i^{\mathrm{AN}} \\ \alpha_i \end{bmatrix} = \left(G_i^T G_i\right)^{-1} G_i^T U_i. \quad (8)$$

Thus, according to the estimated position error, each AN's position can be calibrated using the following equation:

$$\begin{bmatrix} x_i^{\mathrm{AN}} \\ y_i^{\mathrm{AN}} \\ z_i^{\mathrm{AN}} \end{bmatrix} = \begin{bmatrix} \hat{x}_i^{\mathrm{AN}} - \delta\tilde{x}_i^{\mathrm{AN}} \\ \hat{y}_i^{\mathrm{AN}} - \delta\tilde{y}_i^{\mathrm{AN}} \\ \hat{z}_i^{\mathrm{AN}} - \delta\tilde{z}_i^{\mathrm{AN}} \end{bmatrix}. \tag{9}$$

Once the position error and scale-factor error are obtained, the bias can be calculated as follows:

$$R_i = \mathrm{HB}_i + W \tag{10}$$

where

$$R_i = \begin{bmatrix} d_{i-1} - (1+\tilde{\alpha}_i)\sqrt{\left(\tilde{x}_{i-1}^{\mathrm{RN}}\right)^2 + \left(\tilde{y}_{i-1}^{\mathrm{RN}}\right)^2 + \left(\tilde{z}_{i-1}^{\mathrm{RN}}\right)^2} \\ d_{i-2} - (1+\tilde{\alpha}_i)\sqrt{\left(\tilde{x}_{i-2}^{\mathrm{RN}}\right)^2 + \left(\tilde{y}_{i-2}^{\mathrm{RN}}\right)^2 + \left(\tilde{z}_{i-2}^{\mathrm{RN}}\right)^2} \\ \vdots \\ d_{i-n} - (1+\tilde{\alpha}_i)\sqrt{\left(\tilde{x}_{i-n}^{\mathrm{RN}}\right)^2 + \left(\tilde{y}_{i-n}^{\mathrm{RN}}\right)^2 + \left(\tilde{z}_{i-n}^{\mathrm{RN}}\right)^2} \end{bmatrix} \tag{11}$$

$$H = [1, 1, \ldots, 1]^T \tag{12}$$

where

$$\begin{aligned} \tilde{x}_{i-j}^{\mathrm{RN}} &= \hat{x}_i^{\mathrm{AN}} - \delta\tilde{x}_i^{\mathrm{AN}} - x_j^{\mathrm{RN}}, \tilde{y}_{i-j}^{\mathrm{RN}} \\ &= \hat{y}_i^{\mathrm{AN}} - \delta\tilde{y}_i^{\mathrm{AN}} - x_j^{\mathrm{RN}}, \tilde{z}_{i-j}^{\mathrm{RN}} = \hat{z}_i^{\mathrm{AN}} - \delta\tilde{z}_i^{\mathrm{AN}} - x_j^{\mathrm{RN}}. \end{aligned}$$

Hence, the bias of each AN can be calculated as follows:

$$\tilde{B}_i = \left(H^T H\right)^{-1} H^T R_i. \tag{13}$$

B. VBUKF Algorithm

According to the aforementioned presentation, each AN with respect to scale-factor error, bias as well as position error can be calibrated and compensated. For the determined positioning space, upon implementing the calibration, the channel errors could be considered the fixed values. Unfortunately, in the NLOS situation, the bias was difficult to separate from the NLOS error in (2). The NLOS error was closely related to the localization space, giving rise to the uncertain and variable NLOS measurement noise, which meant the bias would need to be estimated in real-time to improve ranging quality. For this purpose, an appropriate filter method should be selected. We used the VBUKF to smooth the NLOS error; that is, we utilized the VB to approximate the dynamical measurement noise and the UKF to update the states.

The ranging state vector at instant k is modeled as follows:

$$D_{m,k} = \left[d_{m,k}, \dot{d}_{m,k}\right]^T \quad m = 1, 2, \ldots, M \tag{14}$$

where $d_{m,k}$ represents the measured distance between the TN and the mth AN; and $\dot{d}_{m,k}$ represents the velocity of the TN.

We consider the following discrete-time state–space model:

$$D_{m,k} = \mathrm{FD}_{m,k-1} + B w_{k-1} \tag{15}$$

$$Z_{m,k} = \mathrm{AD}_{m,k} + \upsilon_k \tag{16}$$

where

$$F = \begin{bmatrix} 1 \Delta T \\ 01 \end{bmatrix}; \quad B = \begin{bmatrix} \Delta T^2/2 \\ \Delta T \end{bmatrix}$$

and $A = [1, 0]$; T stands for sampling interval; w_{k-1} indicates process noise with zero mean and covariance matrices $Qk - 1$; and υ_k is measurement noise with covariance matrices $\hat{R}_k$.

For simplicity, we substituted D_k with $D_{m,k}$. According to [30], with the given observations $Z_{1:k-1}$, the ranging state D_k and unknown measurement noise covariance $\hat{R}_k$ at instant k can be approximated as the product of Gaussian distribution and inverse Wishart (IW) distribution [30], given by

$$\begin{aligned} &p\left(D_k, \hat{R}_k | Z_{1:k-1}\right) \\ &\quad = p(D_k | Z_{1:k-1}) p\left(\hat{R}_k | Z_{1:k-1}\right) \\ &\quad = N\left(D_k | \bar{D}_{k-1|k-1}, P_{k|k-1}\right) IW\left(\hat{R}_k | \hat{\upsilon}_{k|k-1}, V_{k|k-1}\right). \end{aligned} \tag{17}$$

The unknown measurement noise with respect to $\hat{\upsilon}_{k|k-1}$ and $\hat{V}_{k|k-1}$ in the IW distribution can be modeled as follows:

$$\hat{\upsilon}_{k|k-1} = \beta\left(\hat{\upsilon}_{k-1|k-1} - n - 1\right) + n + 1 \tag{18}$$

$$\hat{V}_{k|k-1} = B \hat{V}_{k-1|k-1} B^T \tag{19}$$

where $0 < \beta \leq 1$, $0 < ||B|| < 1$; and n represents the dimension of the measurement vector. According to the VB approximation inference, the joint posterior distribution $p(D_k, \hat{R}_k | Z_{1:k})$ can be approximated and expressed as a factorized form [15]

$$p\left(D_k, \hat{R}_k | Z_{1:k}\right) \approx Q(D_k) Q\left(\hat{R}_k\right). \tag{20}$$

The involved parameters $Q(D_k)$ and $Q(\hat{R}_k)$ can be obtained using the thought of VB approximation by minimizing the Kullback–Leibler (KL) divergence between the posterior approximation distribution and the true distribution [15], given by

$$\begin{aligned} &\mathrm{KL}\left[Q_D(D_k) Q_{\hat{R}}\left(\hat{R}_k\right) \| p\left(D_k, \hat{R}_k | Z_{1:k}\right)\right] \\ &\quad = \int Q_D(D_k) Q_{\hat{R}}\left(\hat{R}_k\right) \times \log\left(\frac{Q_D(D_k) Q_{\hat{R}}\left(\hat{R}_k\right)}{p\left(D_k, \hat{R}_k | Z_{1:k}\right)}\right) dD_k d\hat{R}_k. \end{aligned} \tag{21}$$

By minimizing the KL divergence in (21), we get the following approximation [15]:

$$Q_D(D_k) \propto \exp\left(\int \log p\left(Z_k, D_k, \hat{R}_k | Z_{1:k-1}\right) Q_{\hat{R}}\left(\hat{R}_k\right) d\hat{R}_k\right) \tag{22}$$

$$Q_{\hat{R}}\left(\hat{R}_k\right) \propto \exp\left(\int \log p\left(Z_k, D_k, \hat{R}_k | Z_{1:k-1}\right) Q_D(D_k) dD_k\right). \tag{23}$$

The unknown measurement noise covariance is calculated by using the mean of the IW distribution, given by

$$\hat{R}_k = \left(\hat{\upsilon}_{k|k} - n - 1\right)^{-1} \hat{V}_{k|k}. \tag{24}$$

The procedure of VBUKF worked in the following manner.

1) Time Update: Factorize the covariance using the singular value decomposition (SVD) method, expressed as follows:

$$P_{k-1|k-1} = U_{k-1|k-1} \cdot \Lambda_{k-1|k-1} \cdot C_{k-1|k-1}^T. \tag{25}$$

Compute the sigma points and weight coefficients, as follows:

$$\begin{cases} X_{0,k-1|k-1} = \bar{D}_{k-1|k-1} & \\ X_{l,k-1|k-1} = \bar{D}_{k-1|k-1} + U_{k-1|k-1} & \\ \cdot \left(\sqrt{\Lambda_{k-1|k-1}(n+\lambda)}\right)_l, & l = 1, \ldots, n \\ X_{l,k-1|k-1} = \bar{D}_{k-1|k-1} - U_{k-1|k-1} & \\ \cdot \left(\sqrt{\Lambda_{k-1|k-1}(n+\lambda)}\right)_l, & l = n+1, \ldots, 2n \\ w_0^n = \dfrac{\lambda}{n+\lambda}, w_0^c = \dfrac{\lambda}{n+\lambda} + 1 & \\ + \alpha^2 - \beta, & w_l^n = w_l^c = \dfrac{\lambda}{2(n+\lambda)} \end{cases} \tag{26}$$

where $\lambda = \alpha^2(n+\delta) - n$ is a composite scaling factor, wherein the parameter α $(0 \le \alpha \le 0.5)$ determines the spread rate of the sigma points; and δ is usually set to $3-n$ to decrease the higher-order errors of mean and covariance approximations.

The transformed points yield

$$X^*_{l,k-1|k-1} = F X_{l,k-1|k-1}. \tag{27}$$

Calculate the predicted state mean and covariance matrix

$$\bar{D}_{k|k-1} = \sum_{l=1}^{2n} w_l^n X^*_{l,k-1|k-1} \tag{28}$$

$$P_{k|k-1} = \sum_{l=1}^{2n} w_l^c \left(X^*_{l,k-1|k-1} - \bar{D}_{k|k-1}\right) \cdot \left(X^*_{l,k-1|k-1} - \bar{D}_{k|k-1}\right)^T + Q_k. \tag{29}$$

Calculate the measurement noise as follows:

$$\hat{\upsilon}_{k|k-1} = \beta\left(\hat{\upsilon}_{k-1|k-1} - n - 1\right) + n + 1 \tag{30}$$

$$\hat{V}_{k|k-1} = B \hat{V}_{k-1|k-1} B^T. \tag{31}$$

2) Variational Measurement Update: First, set $\bar{D}^{(0)}_{k|k} = \bar{D}_{k|k}$, $P^{(0)}_{k|k} = P_{k|k}$, $\upsilon_{k|k} = \hat{\upsilon}_{k|k-1} + 1$, $\hat{V}^{(0)}_k = \hat{V}_{k|k-1}$, and then calculate the following:

$$Z_{l,k|k-1} = A X^*_{l,k|k-1} \tag{32}$$

$$\hat{Z}_{k|k-1} = \sum_{l=1}^{2n} w_l^n Z_{l,k|k-1}. \tag{33}$$

Calculate the cross-covariance matrix as follows:

$$P_{XZ,k|k-1} = \sum_{l=1}^{2n} w_l^c \cdot \left(X^*_{l,k-1|k-1} - \bar{D}_{k|k-1}\right)\left(Z_{l,k|k-1} - \hat{Z}_{k|k-1}\right). \tag{34}$$

Calculate the innovation covariance ignoring measurement noise variance matrix as follows:

$$P_{Z,k|k-1} = \sum_{l=1}^{2n} w_l^c \cdot \left(Z_{l,k|k-1} - \hat{Z}_{k|k-1}\right) \cdot \left(Z_{l,k|k-1} - \hat{Z}_{k|k-1}\right)^T. \tag{35}$$

Iterate the following step (N times for $i = 0, 1, \ldots, N$).

Estimate the measurement noise variance matrix

$$\hat{R}_k^{(i)} = \left(\hat{\upsilon}_{k|k} - n - 1\right)^{-1} \hat{V}_k^{(i)}. \tag{36}$$

Estimate the innovation covariance

$$P^{(i+1)}_{ZZ,k|k-1} = P_{Z,k|k-1} + R_k^{(i)}. \tag{37}$$

Calculate the filtering gain as follows:

$$K_k^{(i+1)} = P_{XZ,k|k-1}\left(P^{(i+1)}_{ZZ,k|k-1}\right)^{-1}. \tag{38}$$

Evaluate the update state vector $\bar{D}_{k|k}$ as follows:

$$\bar{D}^{(i+1)}_{k|k} = \bar{D}_{k|k-1} + K_k^{(i+1)}\left(Z_k - \hat{Z}_{k|k-1}\right). \tag{39}$$

Update the estimation error covariance matrix $P_{k|k}$ as follows:

$$P^{(i+1)}_{k|k} = P_{k|k-1} - K_k^{(i+1)} P^{(i+1)}_{ZZ,k|k-1}\left(K_k^{(i+1)}\right)^T. \tag{40}$$

Update the measurement noise parameters

$$\hat{V}_k^{(i+1)} = \hat{V}_{k|k-1} + \sum_{l=1}^{2n} w_l^c \cdot \left(Z_k - A\bar{D}^{(i)}_{k|k}\right)\left(Z_k - A\bar{D}^{(i)}_{k|k}\right)^T. \tag{41}$$

Set $\hat{V}_{k|k} = \hat{V}_k^{(N)}$, $P_{k|k} = P_{k|k}^{(N)}$, $\hat{R}_k = \hat{R}_k^{(N)}$.

Thus, more accurate ranging estimation is formulated as follows:

$$\widehat{d}_{m,k} = A\bar{D}_{k|k}. \tag{42}$$

The whole VBUKF process is provided in Appendix A.

III. Location Calculation

A. Total Least Squares

After the calibration and VBUKF smoother were completed, we were able to attain the more accurate distance estimations, and the position of TN can be estimated using the LS method. The available observation equations of the UWB positioning system composed of four ANs are modeled as follows:

$$\begin{cases} \left(x_1^{\mathrm{AN}} - x\right)^2 + \left(y_1^{\mathrm{AN}} - y\right)^2 + \left(z_1^{\mathrm{AN}} - z\right)^2 = \widehat{d}_1^{\,2} \\ \left(x_2^{\mathrm{AN}} - x\right)^2 + \left(y_2^{\mathrm{AN}} - y\right)^2 + \left(z_2^{\mathrm{AN}} - z\right)^2 = \widehat{d}_2^{\,2} \\ \left(x_3^{\mathrm{AN}} - x\right)^2 + \left(y_3^{\mathrm{AN}} - y\right)^2 + \left(z_3^{\mathrm{AN}} - z\right)^2 = \widehat{d}_3^{\,2} \\ \left(x_4^{\mathrm{AN}} - x\right)^2 + \left(y_4^{\mathrm{AN}} - y\right)^2 + \left(z_4^{\mathrm{AN}} - z\right)^2 = \widehat{d}_4^{\,2} \end{cases} \tag{43}$$

where $\widehat{d}_1, \widehat{d}_2, \widehat{d}_3$, and $\widehat{d}_4$ represent the distance between the TN and corresponding AN after calibration and VBUKF smoothing, respectively; and $(x_i^{\mathrm{AN}}, y_i^{\mathrm{AN}}, z_i^{\mathrm{AN}})$ stands for the coordinates of the ith ANs after calibration compensation with $i = 1, 2, 3, 4$.

Converting (43) into the matrix form yields

$$\mathrm{C}X = S \tag{44}$$

where

$$C = \begin{bmatrix} \left(x_2^{\mathrm{AN}} - x_1^{\mathrm{AN}}\right)\left(y_2^{\mathrm{AN}} - y_1^{\mathrm{AN}}\right)\left(z_2^{\mathrm{AN}} - z_1^{\mathrm{AN}}\right) \\ \left(x_3^{\mathrm{AN}} - x_2^{\mathrm{AN}}\right)\left(y_3^{\mathrm{AN}} - y_2^{\mathrm{AN}}\right)\left(z_3^{\mathrm{AN}} - z_2^{\mathrm{AN}}\right) \\ \left(x_4^{\mathrm{AN}} - x_3^{\mathrm{AN}}\right)\left(y_4^{\mathrm{AN}} - y_3^{\mathrm{AN}}\right)\left(z_4^{\mathrm{AN}} - z_3^{\mathrm{AN}}\right) \end{bmatrix}, \quad X = \begin{bmatrix} x \\ y \\ z \end{bmatrix}$$

$$S = \frac{1}{2}\begin{bmatrix} \left(x_2^{\mathrm{AN}}\right)^2 + \left(y_2^{\mathrm{AN}}\right)^2 + \left(z_2^{\mathrm{AN}}\right)^2 - \left(x_1^{\mathrm{AN}}\right)^2 \\ + \left(y_1^{\mathrm{AN}}\right)^2 + \left(z_1^{\mathrm{AN}}\right)^2 + d_1^2 - d_2^2 \\ \left(x_3^{\mathrm{AN}}\right)^2 + \left(y_3^{\mathrm{AN}}\right)^2 + \left(z_3^{\mathrm{AN}}\right)^2 - \left(x_2^{\mathrm{AN}}\right)^2 \\ + \left(y_2^{\mathrm{AN}}\right)^2 + \left(z_2^{\mathrm{AN}}\right)^2 + d_2^2 - d_3^2 \\ \left(x_4^{\mathrm{AN}}\right)^2 + \left(y_4^{\mathrm{AN}}\right)^2 + \left(z_4^{\mathrm{AN}}\right)^2 - \left(x_3^{\mathrm{AN}}\right)^2 \\ + \left(y_3^{\mathrm{AN}}\right)^2 + \left(z_3^{\mathrm{AN}}\right)^2 + d_3^2 - d_4^2 \end{bmatrix}.$$

The LS solution of the TN is given by

$$X_{\mathrm{LS}} = \left(C^T C\right)^{-1} C^T S. \tag{45}$$

Generally, there was an underlying assumption that all the errors were confined to the observation vector S in the conventional LS problem. Unfortunately, this assumption was usually unrealistic which was due to the fact that matrix C still contained the error caused by an installation error, albeit all the ANs the position errors were calibrated. In practical applications, it was a formidable challenge to obtain the exact coordinates of ANs without error. In the light of this, incorporating the above consideration, we utilized the TLS approach to compute the TN's position while taking into account the error contained in both matrix C and the observation vector S. Thus, (44) is rewritten as follows:

$$\tilde{C}X = \tilde{S}. \tag{46}$$

Simply put, the chief goal of using TLS is to introduce the perturbations C and S into matrix C and S, respectively, to correct for their corresponding noise, expressed as follows:

$$(C + \Delta C)X = S + \Delta S. \tag{47}$$

Equation (47) can be expressed in the following form:

$$(B + M)Y = 0 \tag{48}$$

where

$$B = [C|S], \quad M = [\Delta C|\Delta S], \quad Y = [X, -1]^T.$$

According to [44], the solution of the TLS approach can be derived using the SVD of B, which is given by

$$B = U \Sigma V^H \tag{49}$$

where $U = (u_1, u_2, \ldots, u_m)$; $\sum = \mathrm{diag}(\sigma_1, \sigma_2, \ldots, \sigma_{L+1})$; $V = (v_1, v_2, \ldots, v_{L+1})$; and $v_{L+1} = (v_{1,L+1}, v_{2,L+1}, \ldots, v_{L+1,L+1})$; U and V indicate unitary matrices; $\sum$ represents a diagonal matrix, whose diagonal elements σ_L are arranged in the descending order; L indicates the number of the estimated parameter, namely, $L = 3$.

Thus, the TLS solution can be obtained from [44]

$$X_{TLS} = -\frac{1}{v_{L+1,L+1}}\left(v_{1,L+1}, v_{2,L+1}, \ldots, v_{L,L+1}\right). \tag{50}$$

B. Water Cycle Algorithm

Although the location coordinates of the TN can be estimated reliably using the TLS method after implementing the proposed calibration and VBUKF smoothing, the process produced unavoidable errors during TLS linearization. Fortunately, there exist many available and appropriate optimization approaches to improve positioning accuracy, which can be divided into iterative and noniterative algorithms. One iterative approach that has proven effective is the GNA, however, it is sensitive to initial estimates, and its precision might perform poorly when the initially estimated values possess high degrees of error. The goal of the noniterative algorithm was to minimize the objective function to optimize the position estimate, such as WCA, particle swarm optimization (PSO), ant colony optimization (ACO), genetic algorithm (GA), and mine blast algorithm (MBA). The WCA is an intelligence optimization algorithm initially developed by Sadollah *et al.* [45], which was enlightened by the natural phenomena of the water cycle process and how rivers and streams flow to the sea and have been proven to have the ability to compete with other metaheuristic algorithms [46] . Additionally, the WCA is particularly useful in finding optimal solutions as well as the fast convergence ability. Thus, the WCA method was implemented in this study to improve the positioning accuracy due to its ability to effectively find optimization solutions approaching the global optimum [45]. To successfully obtain the TN's optimum solution with the lowest errors, the objective function is formulated as follows:

$$f(X) = \sum_{i=1}^{4}\left\{\sqrt{\left(x - x_i^{\mathrm{AN}}\right)^2 + \left(y - y_i^{\mathrm{AN}}\right)^2 + \left(z - z_i^{\mathrm{AN}}\right)^2} - \widehat{d}_i\right\}^2 \tag{51}$$

where (x, y, z) indicates the TN's position obtained from the UTLS and CTLS approaches, and $\widehat{d}_i$ represents the measured distance after calibration and VBUKF smoothing. According to the reasoning of the WCA method, the procedure of WCA was broken down into the following predominant steps.

1) Randomly generate the populations of raindrops within the positioning space and form the initial sea, rivers, and streams, given as follows:

$$\mathrm{Raindrops} = \begin{bmatrix} \mathrm{Sea} \\ \mathrm{River}_1 \\ \vdots \\ \mathrm{Stream}_{N_{sr+1}} \\ \vdots \\ \mathrm{Stream}_N \end{bmatrix} = \begin{bmatrix} x_1 & y_1 & z_1 \\ x_2 & y_2 & z_2 \\ x_3 & y_3 & z_3 \\ \vdots & \vdots & \vdots \\ x_N & y_N & z_N \end{bmatrix}. \tag{52}$$

2) Calculate the fitness value of streams using (51).
3) Calculate the corresponding flow intensities of rivers and sea based on the following equation:

$$\mathrm{NS}_n = \mathrm{round}\left\{\left|\frac{\mathrm{Fitness}_n}{\sum_{i=1}^{N_{sr}} \mathrm{Fitness}_i}\right| \times N_{\mathrm{Raindrops}}\right\}, \quad n = 1, 2, \ldots, N_{sr}. \tag{53}$$

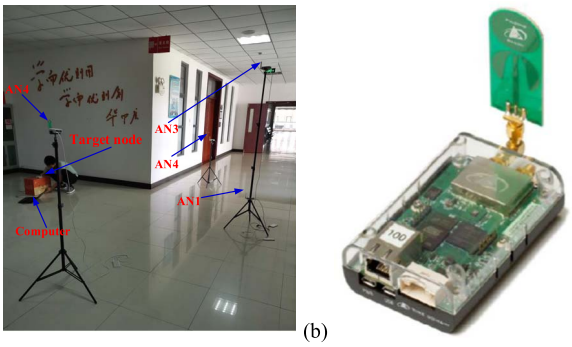

Fig. 1. (a) Localization experiment environment. (b) UWB P440 module.

TABLE I
SPECIFICATIONS OF THE UWB p440

Specification	Value
Input power	5 V
Center frequency	4.3 GHz
measurement accuracy	50 px
transmitting power	50 μW
Maximum refresh rate	125 Hz
Radio frequency	3.1 – 4.8 GHz
Maximum baud rate	19.2 – 612 kbp

4) Streams flow into the sea and rivers using the following rules:

$$X_{\text{Stream}}^{t+1} = X_{\text{Stream}}^{t} + \text{rand} \times C \times \left(X_{\text{Sea}}^{t} - X_{\text{Stream}}^{t}\right) \quad (54)$$

$$X_{\text{Stream}}^{t+1} = X_{\text{Stream}}^{t} + \text{rand} \times C \times \left(X_{\text{River}}^{t} - X_{\text{Stream}}^{t}\right). \quad (55)$$

5) Rivers flow into the sea based on the following:

$$X_{\text{River}}^{t+1} = X_{\text{River}}^{t} + \text{rand} \times C \times \left(X_{\text{Sea}}^{t} - X_{\text{River}}^{t}\right). \quad (56)$$

6) Check the evaporative conditions using the following rule:

$$\left|X_{\text{Sea}}^{t} - X_{\text{River},j}^{t}\right| < d_{\max} \text{ or } \text{rand} < 0.1 \quad j = 1, \ldots, \text{N}_{\text{sr}} - 1. \quad (57)$$

If the conditions facilitated evaporation, the raining process occurs and new streams are formed based on the following equation:

$$X_{\text{Stream}}^{\text{new}} = X_{\text{Sea}} + \sqrt{\mu} \times \text{rand}\, n(1, 3). \quad (58)$$

7) The value of $d_{\max}$ adaptively decreases over the iterations, given by

$$d_{\max}^{t+1} = d_{\max}^{t} - \frac{d_{\max}^{t}}{\text{MaxG}}. \quad (59)$$

8) Determine whether the maximum iteration times are satisfied. If no, let $t = t + 1$, and skip to step 3).
If yes, the optimal solution of TN can be obtained, expressed as follows:

$$X_{\text{Sea\_best}} = (x_b, y_b, z_b). \quad (60)$$

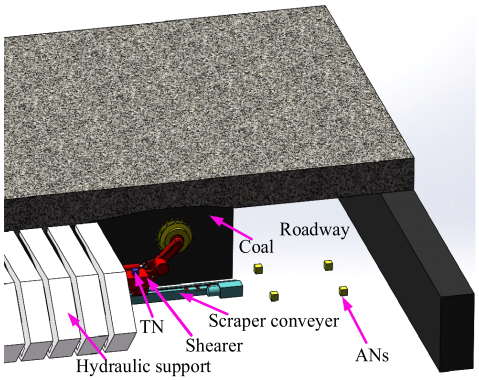

Fig. 2. Arrangement of the P440 sensors at the end of the FMMF.

IV. EXPERIMENTAL SETUP AND RESULTS

A. Experimental Setup

The UWB P440 module, which uses two-way time-of-flight distance measurement, was manufactured by the American Time Domain Company, Huntsville, AL, USA [47], as illustrated in Fig. 1(b), and its leading performance parameters are summarized in Table I. The P440 module was chosen to serve as the TN and ANs owing to its high performance and reliability. For the purpose of obtaining the shearer's location information, it has been proposed that the TN should be installed on the shearer body, and the four ANs be mounted on the top and bottom of hydraulic supports [12]. Nevertheless, this approach was still limited by the difficulty of accurately determining the locations of four ANs because the hydraulic support system frequently moved forward, degrading positioning performance by a large margin. Hence, in this article, we suggested that the four ANs be installed at the end of the FMMF to calculate the shearer's position coordinates, as depicted in Fig. 2.

To validate the effectiveness and adaptability of the proposed calibration compensation and VBUKF smoothing approach, our experiments were conducted on the floor of a building in the China University of Mining and Technology, XuZhou, China. To better test the shearer localization using the UWB positioning system and simulate the existence of the NLOS situation, one AN was deployed in an NLOS position to generate the NLOS ranging data, similar to the arrangement during the static and dynamic positioning experiments to simulate NLOS scenarios. The four ANs were configured into a V-shape deployment pattern [15], and the experiment layout was provided in Fig. 1(a), which was certified that this arrangement benefitted to achieve a relatively accurate estimation. Fig. 3 displays the ANs deployment and movement trajectories, where the arrows indicate the TN's movement direction. For the static experiment, we selected a localization point every 0.15 m along the set trajectory; and there were 19 positioning points in total with 300 ranging data collected at each. In the dynamic experiment, the TN moved along the set trajectory. The ANs were fixed on tripods with the position coordinates AN1 (3.636, 6.102, 0.478), AN2 (5.983, 4.796, 1.097), AN3 (3.588, 6.033, 2.179), and AN4 (1.208, 4.799, 1.440).

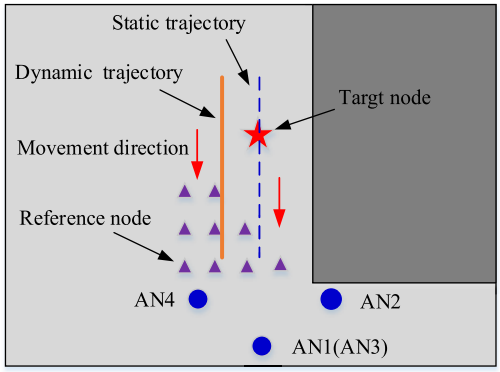

Fig. 3. Schematic of ANs and RNs deployment and static and dynamic movement trajectories in the evaluation scenario.

TABLE II
SCALE-FACTOR ERROR, BIAS, AND COORDINATES OF ANS AFTER CALIBRATION

AN	Scale factor error	Bias	Coordinates
AN1	0.018	-0.0933	(3.641, 6.052, 0.483)
AN2	-0.022	0.0852	(6.005, 4.802, 1.091)
AN3	0.0031	-0.0272	(3.603, 6.045, 2.183)
AN4	-0.029	0.0789	(1.203, 4.802, 1.443)

B. Results Analysis

In order to highlight the superiority of the proposed technique, we adopted the widely utilized root-mean-square error (RMSE), and absolute error concerning x-, y-, and z- as predominant indicators to assess positioning performance, formulated as follows:

$$\text{RMSE} = \sqrt{(x_t - x_r)^2 + (y_t - y_r)^2 + (z_t - z_r)^2} \tag{61}$$

$$\begin{cases} \Delta x = |x_t - x_r| \\ \Delta y = |y_t - y_r| \\ \Delta z = |z_t - z_r| \end{cases} \tag{62}$$

where (x_t, y_t, z_t) indicates the TN's position as calculated using the positioning algorithms in this article; and (x_r, y_r, z_r) stands for the TN's actual position coordinates.

According to the position of the ANs, nine RNs with appropriate and reasonable positions were selected within the positioning space, and the positions were chosen to ensure the transmission channels between the nine RNs and each ANs were LOS, as depicted in Fig. 3. We can compute scale-factor error as well as a bias for each AN using the aforementioned calibration approach, and then the coordinates of each AN can be compensated using the corresponding position error, as displayed in Table II.

In order to explore the effectiveness of the proposed VBUKF smoothing method in NLOS error elimination, Fig. 4 shows the initial ranging data from AN2 at the first localization point and the VBUKF smoothing results. It was clearly visible that the initial measurement distances fluctuated considerably due to the NLOS condition. If we directly utilized the average estimation of these initial ranging data to determine the TN's position, it would yield unreliable estimations with large

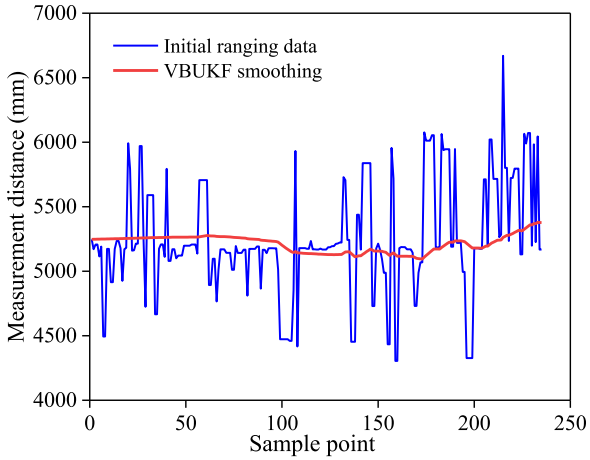

Fig. 4. Measurement distances using VBUKF smoothing.

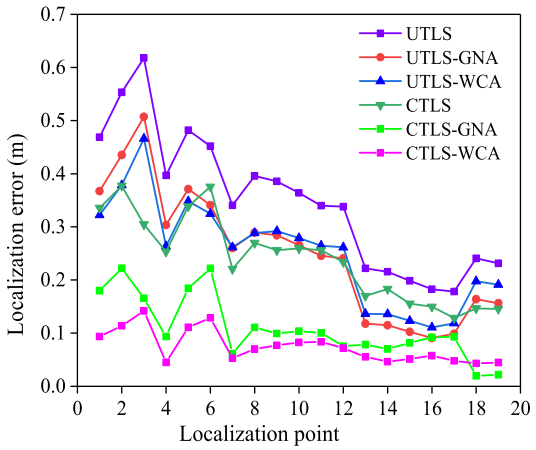

Fig. 5. Comparison of localization error using UTLS, UTLS-GNA, UTLS-WCA, CTLS, CTLS-GNA, and CTLS-WCA methods for the static experiment.

localization errors. Fortunately, after the implementation of the proposed VBUKF smoothing strategy, the fluctuation of estimated distance was significantly reduced, which revealed that the VBUKF enhanced the ranging quality and ameliorated the positioning accuracy and reliability of the UWB system.

To highlight the rationality and adaptability of the proposed CTLS-WCA scheme, the GNA was also applied to optimize the result of the TLS method. The algorithms were tested using data before and after implementation of the calibration to further investigate comprehensively the advantages of the proposed CTLS-WCA technique. For clarity, we used "U" and "C" to differentiate between before and after implementation of the calibration technique resulting in the following notation for the algorithms: UTLS, UTLS-GAN, UTLS-WCA CTLS-WCA, and CTLS, CTLS-GAN, CTLS-WCA, respectively.

The comparison between the TN position estimation errors produced by different positioning methods during the evaluation experiments is unfolded in Fig. 5. It can be seen intuitively that the CTLS-WCA with lower localization error was relatively superior to other compared methods, whereas the TLS possessed a larger positioning error making its positioning

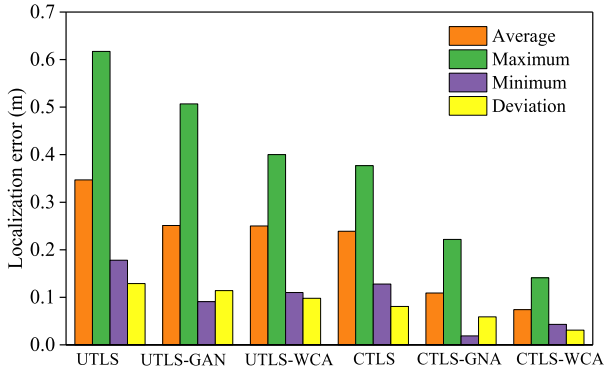

Fig. 6. Maximum, average, minimum, and standard deviation of location estimation error scoured from different methods in the static experiment.

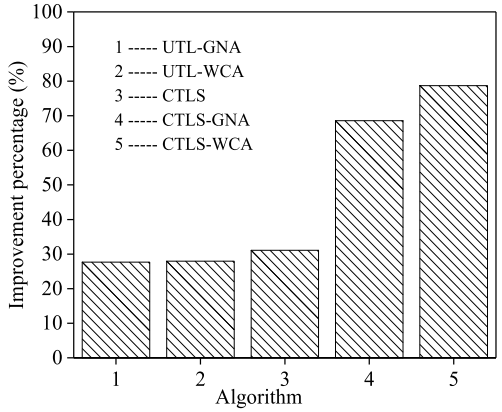

Fig. 7. Average localization accuracy expressed as improvement percentage relative to the TLS method for static experiment.

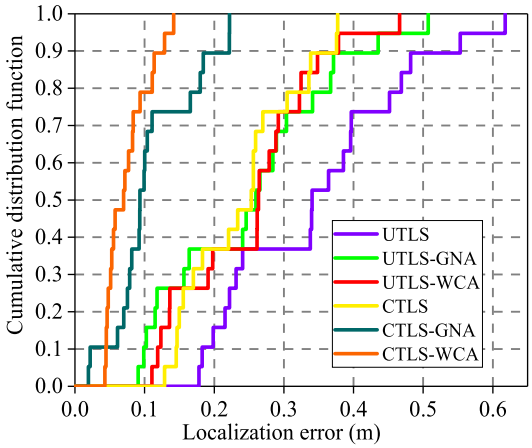

Fig. 8. CDF of localization errors sourced from different methods in the static experiment.

performance unacceptable without implementing calibration and VUBKF smoothing. The AN's position error can be compensated using the proposed calibration method and the NLOS error was able to be eliminated employing the VBUKF smoothing, which enabled the CTLS approach to produce higher localization accuracy than the TLS method. Another observation we can make from these results was that, although positioning accuracy was improved by employing GNA and WCA techniques in the absence of calibration and VBUKF smoothing, the accuracy improvement was not sufficient for field applications. After implementing the proposed calibration and VBUKF smoothing techniques, the CTLS-GNA and CTLS-WCA can return lower positioning errors compared to the corresponding UTLS-GNA and UTLS-WCA methods, indicating that the GNA and WCA techniques were able to further decrease localization error efficiently and effectively and enhance the estimation accuracy. Notably, the positioning error of the CTLS-WCA method was not only much smaller than that of the CTLS-GNA approach, but also possessed less fluctuation in positioning error, highlighting its superior localization performance and robustness, making it more suitable for underground applications.

Descriptive statistics concerning a number of the overall quantitative indexes including the average, minimum, maximum, and standard deviation of positioning error sourced from the mentioned localization methods before and after calibration and VBUKF smoothing were calculated, as displayed in Fig. 6. From these results, it can be seen that the average positioning accuracy of the proposed CTLS-WCA scheme was the highest of all methods, which was up to 0.074 m, CTLS-GNA was the second best with an accuracy of 0.109 m; and the average positioning accuracy of UTLS, UTLS-GNA, UTLS-WCA, as well as CTLS was 0.347, 0.251, 0.250, and 0.239 m, respectively, all of which were greater than 0.2 m. Moreover, the variance in localization error of the CTLS-WCA approach was the lowest, revealing that a more stable localization result can be achieved as contrasted with the other positioning algorithms.

In order to provide a more detailed investigation involving the enhancement performance of the proposed calibration and optimization methodology, we computed the average improvement in localization accuracy of each method relative to the TLS approach, as displayed in Fig. 7. It can be clearly observed that the UTLS-GNA, UTLS-WCA, CTLS, CTLS-GNA, and CTLS-WCA approaches improved the average positioning accuracy by 27.66%, 27.95%, 31.12%, 68.58%, and 78.67%, respectively. Undoubtedly, the average positioning accuracy of the CTLS-GNA and CTLS-WCA methods, after calibration and VBUKF smoothing and implementation of the optimization algorithm, was dramatically higher than the other algorithms. Furthermore, note that the average accuracy of the CTLS-WCA approach possessing superior performance improvement was larger than that of the CTLS-GNA approach, demonstrating that the WCA was the preferable optimization algorithm than the GNA.

The cumulative distribution function (CDF) of the localization errors sourced from the results of the aforementioned positioning approaches is depicted in Fig. 8. Again, the CTLS-WCA possessed the lowest localization error and proved superior to the other mentioned approaches. More specifically, the localization errors were approximately 0.5532, 0.4353, 0.3785, 0.3754, 0.2217, and 0.1286 m, respectively, corresponding to UTLS, UTLS-GNA, UTLS-WCA, CTLS, CTLS-GNA, and CTLS-WCA technique, as the CDF was as high as 90%, which indicated that the calibration and VBUKF

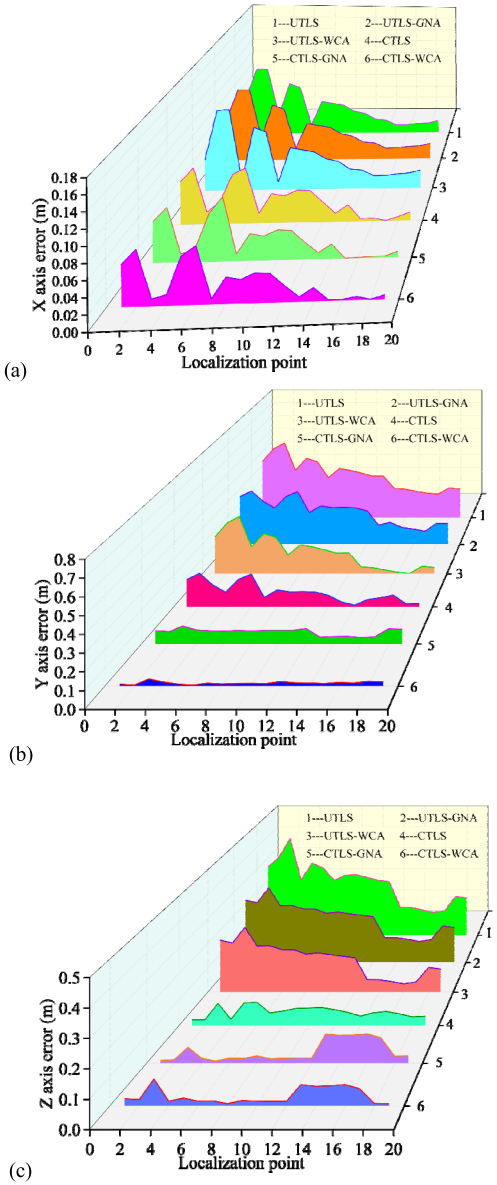

Fig. 9. Localization error distribution on three axes sourced from different methods for static experiment. (a) x-axis error. (b) y-axis error. (c) z-axis error.

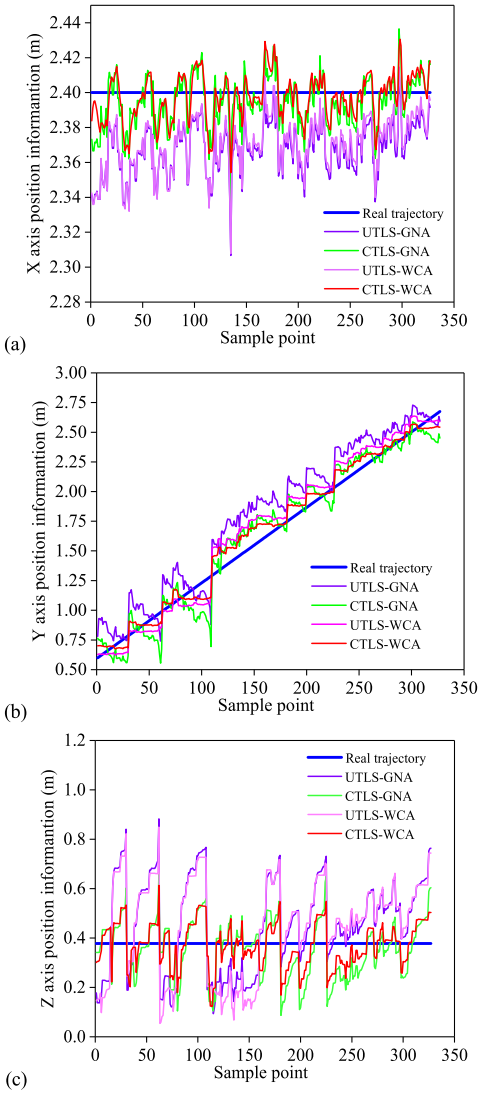

Fig. 10. Dynamic movement trajectories on three axes obtained from UTLS-GNA, CTLS-GNA, UTLS-WCA, and CTLS-WCA approaches. (a) x-axis error. (b) y-axis error. (c) z-axis error.

smoothing can efficiently reduce the localization error and the WCA was best able to optimize the positioning results, enabling CTLS-WCA method to outperform other methods and provide a more accurate estimate result with strong robustness.

To gain further insight into the localization performance as the proposed calibration and VBUKF smoothing are implemented along with the various optimization methods, the positioning error distribution of three coordinate axes are exhibited in Fig. 9. According to these results, it was straightforward to see that the aforementioned positioning approaches had different localization accuracy on all three axes. The positioning performance of TLS, TLS-GAN, and TLS-WCA after implementation of the proposed calibration and VBUKF smoothing on three axes were all obviously superior to UCTLS, UCTLS-GAN, and UTLS-WCA on all three axes, indicating that calibration played a significant role in enhancing positioning accuracy. The localization accuracy of the y- and z-axes were both obviously larger than that of the x-axis before implementing calibration and VBUKF smoothing, which meant the majority of the overall positioning error originated from the y- and z-axes. Calibration and VBUKF smoothing decreased the average positioning error of the x-, y-, and z-axes from 0.0424, 0.3148, and 0.2341 to 0.0317, 0.0916, and 0.0527 m, respectively, whose corresponding average localization accuracy was improved by 25.24%, 70.90%, 77.48%. Furthermore, when the GNA was executed to optimize the outcomes obtained from the CTLS method, the average positioning accuracy of the x-, y-, and z-axes were improved by 13.25%, 21.94%, and 20.11%, respectively; while for WCA, the average positioning accuracy was improved by 20.82%, 81.33%, and 36.24%, respectively. It was worth noting that, although the GAN approach was able to optimize the positioning results on all three axes, the achieved accuracy of WCA optimization was higher than that of the GNA, bringing improvements in the average accuracy up to 40.80%,

94.56%, and 85.64% on the x-, y-, and z-axes, respectively. These improvements made the CTLS-WCA an effective and robust optimization scheme, possessing remarkable advantages over the other approaches.

To further validate the adaptability and usefulness of the proposed calibration and VBUKF smoothing approach, we computed the coordinate of the dynamic trajectory exploiting the proposed technique, as shown in Fig. 10. After the implementation of calibration and VBUKF smoothing, the fluctuation in the position estimates of TN on the three axes was significantly reduced, and the TN's calculated motion trajectory was close to the actual trajectory, which certified that the calibration and VBUKF method proposed in this article can effectively diminish the positioning error and improve the accuracy of dynamic positioning. Furthermore, the trajectory calculated by the CTLS-WCA method was much closer to the actual trajectory than that of the CTLS-GNA approach, further verifying the outstanding positioning performance and robustness of this method, which was consistent with the above conclusions. Based on the comparative analysis of static and dynamic experimental results, we can conclude that the proposed CTLS-WCA technique was able to achieve higher accuracy and efficiency in terms of localization.

V. Conclusion

To eliminate the influence of ANs position error and NLOS error, in this study, we proposed a novel localization scheme based on calibration, VBUKF smoothing and TLS-WCA optimization to ameliorate the estimation accuracy of the UWB positioning system in a complicated underground environment. By utilizing the proposed calibration strategy, the more accurate calibration was achieved through the selection of appropriate RNs in the LOS scenario, enabling accurate estimates of scale-factor error and bias in addition to ANs position errors. In the NLOS condition, due to the difficulty in separating bias and NLOS error, VBUKF smoothing with the consideration of time-variant measurement noise was required to filter the NLOS error. Then, based on the smoothed distance from the VBUKF and position coordinates of ANs after calibration, the TLS method was utilized to estimate the position of the TN, and moreover, the WCA was executed to optimize the estimation result. Static and dynamic experiments were conducted to demonstrate the superiority and effectiveness of applying the proposed TLS-WCA scheme to the UWB positioning system. The experimental result showed that, after calibration and VBUKF smoothing, the estimation accuracy and robustness of the proposed TLS-WCA approach outperformed the other compared method, and the overall average positioning accuracy was improved by 78.67%, and the improvement percentage in accuracy on the x-, y-, and z-axes achieved 40.80%, 94.56%, and 85.64%, respectively. Furthermore, the calculated trajectory of the CTLS-WCA method fluctuated only slightly and was much closer to the actual trajectory than those of other algorithms, exhibiting the superior positioning performance and robustness of this method, and further certifying that the proposed scheme was able to realize the effective and remarkable improvement in terms of localization accuracy.

TABLE III
Implementation VBUKF Algorithm

Initialization:

Set $\bar{D}_{0|0}$, $P_{0|0}$, $\hat{v}_{0|0}$, $\hat{V}_{0|0}$,and calculate the transformed points using the equation (26)-(28).

Time update:

$$\bar{D}_{k|k-1} = \sum_{l=1}^{2n} w_l^n X^*_{l,k-1|k-1}$$

$$P_{k|k-1} = \sum_{l=1}^{2n} w_l^c (X^*_{l,k-1|k-1} - \bar{D}_{k|k-1}) \bullet (X^*_{l,k-1|k-1} - \bar{D}_{k|k-1})^T + Q_k$$

$$\hat{v}_{k|k-1} = \beta(\hat{v}_{k-1|k-1} - n - 1) + n + 1$$

$$\hat{V}_{k|k-1} = B\hat{V}_{k-1|k-1}B^T$$

Variational Measurement update:

Set $\bar{D}^{(0)}_{k|k} = \bar{D}_{k|k}$, $P^{(0)}_{k|k} = P_{k|k}$, $\hat{v}_{k|k} = \hat{v}_{k|k-1} + 1$, $\hat{V}^{(0)}_k = \hat{V}_{k|k}$, and then compute the following:

$$\hat{Z}_{k|k-1} = \sum_{l=1}^{2n} w_l^n A X^*_{l,k|k-1}$$

$$P_{XZ,k|k-1} = \sum_{l=1}^{2n} w_l^c \bullet (X^*_{l,k-1|k-1} - \bar{D}_{k|k-1})(Z_{l,k|k-1} - \hat{Z}_{k|k-1})$$

$$P_{Z,k|k-1} = \sum_{l=1}^{2n} w_l^c \bullet (Z_{l,k|k-1} - \hat{Z}_{k|k-1}) \bullet (Z_{l,k|k-1} - \hat{Z}_{k|k-1})^T$$

For $i = 0 : N-1$

$$\hat{R}_k^{(i)} = (\hat{v}_{k|k} - n - 1)^{-1} \hat{V}_k^{(i)}$$

$$P^{(i+1)}_{ZZ,k|k-1} = P_{Z,k|k-1} + R_k^{(i)}$$

$$K_k^{(i+1)} = P_{XZ,k|k-1} (P^{(i+1)}_{ZZ,k|k-1})^{-1}$$

$$\bar{D}^{(i+1)}_{k|k} = \bar{D}_{k|k-1} + K_k^{(i+1)} (Z_k - \hat{Z}_{k|k-1})$$

$$P^{(i+1)}_{k|k} = P_{k|k-1} - K_k^{(i+1)} P^{(i+1)}_{ZZ,k|k-1} (K_k^{(i+1)})^T$$

$$\hat{V}_k^{(i+1)} = \hat{V}_{k|k-1} + \sum_{l=1}^{2n} w_l^c \bullet (Z_k - A\bar{D}^{(i)}_{k|k})(Z_k - A\bar{D}^{(i)}_{k|k})^T$$

end for

Set $\hat{V}_{k|k} = \hat{V}_k^{(N)}$, $P_{k|k} = P^{(N)}_{k|k}$, $\hat{R}_k = \hat{R}_k^{(N)}$.

Output: $\bar{D}_{k|k}$, $P_{k|k}$, $\hat{v}_{k|k}$, $\hat{V}_{k|k}$, $\hat{R}_{k|k}$

Appendix A

See Table III.

Appendix B

The Taylor series first-order expansion is implemented at the point $(\hat{x}_i^{\mathrm{AN}}, \hat{y}_i^{\mathrm{AN}}, \hat{z}_i^{\mathrm{AN}})$ is expressed as follows:

$$\begin{aligned} d_{i-j} - d_{i-C} \cong\ & (1+\alpha_i)\left(\hat{d}_{i-j} - \frac{\hat{x}_i^{\mathrm{AN}} - x_j^{\mathrm{RN}}}{\hat{d}_{i-j}}\delta x_i^{\mathrm{AN}} \right. \\ & \left. - \frac{\hat{y}_i^{\mathrm{AN}} - y_j^{\mathrm{RN}}}{\hat{d}_{i-j}}\delta y_i^{\mathrm{AN}} - \frac{\hat{z}_i^{\mathrm{AN}} - z_j^{\mathrm{RN}}}{\hat{d}_{i-j}}\delta z_i^{\mathrm{AN}}\right) \\ & -(1+\alpha_i)\left(\hat{d}_{i-c} - \frac{\hat{x}_i^{\mathrm{AN}} - x_c^{\mathrm{RN}}}{\hat{d}_{i-c}}\delta x_i^{\mathrm{AN}} \right. \\ & \left. - \frac{\hat{y}_i^{\mathrm{AN}} - y_c^{\mathrm{RN}}}{\hat{d}_{i-c}}\delta y_i^{\mathrm{AN}} - \frac{\hat{z}_i^{\mathrm{AN}} - z_c^{\mathrm{RN}}}{\hat{d}_{i-c}}\delta z_i^{\mathrm{AN}}\right) + w_i \\ \cong\ & \hat{d}_{i-j} - \hat{d}_{i-c} + (\hat{d}_{i-j} - \hat{d}_{i-c})\alpha_i \\ & - \left(\frac{\hat{x}_i^{\mathrm{AN}} - x_j^{\mathrm{RN}}}{\hat{d}_{i-j}} - \frac{\hat{x}_i^{\mathrm{AN}} - x_c^{\mathrm{RN}}}{\hat{d}_{i-c}}\right)\delta x_i^{\mathrm{AN}} \end{aligned}$$

$$-\left(\frac{\hat{y}_i^{\mathrm{AN}}-y_j^{\mathrm{RN}}}{\hat{d}_{i-j}}-\frac{\hat{y}_i^{\mathrm{AN}}-y_c^{\mathrm{RN}}}{\hat{d}_{i-c}}\right)\delta y_i^{\mathrm{AN}}$$
$$-\left(\frac{\hat{z}_i^{\mathrm{AN}}-z_j^{\mathrm{RN}}}{\hat{d}_{i-j}}-\frac{\hat{z}_i^{\mathrm{AN}}-z_c^{\mathrm{RN}}}{\hat{d}_{i-c}}\right)\delta z_i^{\mathrm{AN}}+w_i.$$

REFERENCES

[1] W. Shibo, Z. Boyuan, W. Shijia, and G. Shirong, "Dynamic precise positioning method of shearer based on closing path optimal estimation model," *IEEE Trans. Autom. Sci. Eng.*, vol. 16, no. 3, pp. 1468–1475, Jul. 2019.

[2] K. Cenacewicz and A. Katunin, "Modeling and simulation of longwall scraper conveyor considering operational faults," *Studia Geotechnica et Mechanica*, vol. 38, no. 2, pp. 15–27, Jun. 2016.

[3] J. C. Xie, Z. J. Yang, X. W. Wang, and S. P. Wang, "A joint positioning and attitude solving method for shearer and scraper conveyor under complex conditions," *Math. Prob. Eng.*, vol. 2017, Oct. 2017, Art. no. 3793412.

[4] G. A. Einicke, J. C. Ralston, C. Hargrave, D. C. Reid, and D. W. Hainsworth, "Longwall mining automation an application of minimum-variance smoothing [Applications of Control]," *IEEE Control Syst. Mag.*, vol. 28, no. 6, pp. 28–37, Dec. 2008.

[5] Q. Tian, Z. Salcic, K. I. K. Wang, and Y. Pan, "A multi-mode dead reckoning system for pedestrian tracking using smartphones," *IEEE Sensors J.*, vol. 16, no. 7, pp. 2079–2093, Apr. 2016.

[6] J. Li, Z. Zeng, J. Sun, and F. Liu, "Through-wall detection of human being's movement by UWB radar," *IEEE Geosci. Remote Sens. Lett.*, vol. 9, no. 6, pp. 1079–1083, Nov. 2012.

[7] L. Yang and G. B. Giannakis, "Ultra-wideband communications: An idea whose time has come," *IEEE Signal Process. Mag.*, vol. 21, no. 6, pp. 26–54, Nov. 2004.

[8] J. A. Corrales, F. A. Candelas, and F. Torres, "Sensor data integration for indoor human tracking," *Robot. Auto. Syst.*, vol. 58, no. 8, pp. 931–939, Aug. 2010.

[9] J. D. Hol, F. Dijkstra, H. Luinge, and T. B. Schon, "Tightly coupled UWB/IMU pose estimation," in *Proc. IEEE Int. Conf. Ultra-Wideband*, Sep. 2009, pp. 688–692.

[10] S. Zihajehzadeh, P. K. Yoon, B.-S. Kang, and E. J. Park, "UWB-aided inertial motion capture for lower body 3-D dynamic activity and trajectory tracking," *IEEE Trans. Instrum. Meas.*, vol. 64, no. 12, pp. 3577–3587, Dec. 2015.

[11] M. G. Li, H. Zhu, S. Z. You, L. Wang, and Z. C. Q. Zhang Tang, "IMU-aided ultra-wideband based localization for coal mine robots," in *Proc. Int. Conf. Intell. Robot. Appl.*, Shenyang, China, Aug. 2019, pp. 256–268.

[12] Q. Fan *et al.*, "Integrated positioning for coal mining machinery in enclosed underground mine based on SINS/WSN," *Sci. World J.*, vol. 2014, Jan. 2014, Art. no. 460415.

[13] J. Wang, Y. Gao, Z. Li, X. L. Meng, and C. M. Hancock, "A tightly-coupled GPS/INS/UWB cooperative positioning sensors system supported by V2I communication," *Sensors*, vol. 16, no. 7, p. 994, Jun. 2016.

[14] Q. Tian, K. I.-K. Wang, and Z. Salcic, "A low-cost INS and UWB fusion pedestrian tracking system," *IEEE Sensors J.*, vol. 19, no. 10, pp. 3733–3740, May 2019.

[15] B. Cao, S. Wang, S. Ge, X. Ma, and W. Liu, "A novel mobile target localization approach for complicate underground environment in mixed LOS/NLOS scenarios," *IEEE Access*, vol. 8, pp. 96347–96362, 2020.

[16] V. Savic, E. G. Larsson, J. Ferrer-Coll, and P. Stenumgaard, "Kernel methods for accurate UWB-based ranging with reduced complexity," *IEEE Trans. Wireless Commun.*, vol. 15, no. 3, pp. 1783–1793, Mar. 2016.

[17] J. Zhang, J. Salmi, and E.-S. Lohan, "Analysis of kurtosis-based LOS/NLOS identification using indoor MIMO channel measurement," *IEEE Trans. Veh. Technol.*, vol. 62, no. 6, pp. 2871–2874, Jul. 2013.

[18] K. Yu and Y. J. Guo, "Statistical NLOS identification based on AOA, TOA, and signal strength," *IEEE Trans. Veh. Technol.*, vol. 58, no. 1, pp. 274–286, Jan. 2009.

[19] K. K. Cwalina, P. Rajchowski, O. Blaszkiewicz, A. Olejniczak, and J. Sadowski, "Deep learning-based LOS and NLOS identification in wireless body area networks," *Sensors*, vol. 19, no. 19, p. 4229, Sep. 2019.

[20] Z. Xiao, H. Wen, A. Markham, N. Trigoni, P. Blunsom, and J. Frolik, "Non-line-of-sight identification and mitigation using received signal strength," *IEEE Trans. Wireless Commun.*, vol. 14, no. 3, pp. 1689–1702, Mar. 2015.

[21] S. Venkatraman, J. Caffery, and H.-R. You, "A novel ToA location algorithm using LoS range estimation for NLoS environments," *IEEE Trans. Veh. Technol.*, vol. 53, no. 5, pp. 1515–1524, Sep. 2004.

[22] J. Borras, P. Hatrack, and N. B. Mandayam, "Decision theoretic framework for NLOS identification," in *Proc. 48th IEEE Veh. Technol. Conf. Pathway Global Wireless Revolution*, vol. 2, May 1998, pp. 1583–1587.

[23] P.-C. Chen, "A non-line-of-sight error mitigation algorithm in location estimation," in *Proc. IEEE Wireless Commun. Netw. Conf.*, Sep. 1999, pp. 316–320.

[24] Y. Wang, Y. Jing, and Z. Jia, "An indoor mobile localization strategy for robot in NLOS environment," *Int. J. Distrib. Sensor Netw.*, vol. 2013, pp. 1–8, Jan. 2013.

[25] S. Venkatesh and R. M. Buehrer, "NLOS mitigation using linear programming in ultrawideband location-aware networks," *IEEE Trans. Veh. Technol.*, vol. 56, no. 5, pp. 3182–3198, Sep. 2007.

[26] A. Ribeiro, I. D. Schizas, S. Roumeliotis, and G. B. Giannakis, "Kalman filtering in wireless sensor networks," *IEEE Control Syst.*, vol. 30, no. 2, pp. 66–86, Apr. 2010.

[27] N. Modalavalasa, G. S. B. Rao, K. S. Prasad, L. Ganesh, and M. N. V. S. S. Kumar, "A new method of target tracking by EKF using bearing and elevation measurements for underwater environment," *Robot. Auton. Syst.*, vol. 74, pp. 221–228, Dec. 2015.

[28] Z. Zhang, N. Hu, Y. Guo, and X. Yang, "The NLOS localization algorithm based on the linear regression model of hybrid filter," in *Proc. Chin. Control Decis. Conf. (CCDC)*, Nanchang, China, Jun. 2019, pp. 2442–2445.

[29] L. Cheng, Y. Li, Y. Wang, Y. Bi, L. Feng, and M. Xue, "A triple-filter NLOS localization algorithm based on fuzzy C-means for wireless sensor networks," *Sensors*, vol. 19, no. 5, p. 1215, Mar. 2019.

[30] J. Wang, T. Zhang, X. Xu, and Y. Li, "A variational Bayesian based strong tracking interpolatory cubature Kalman filter for maneuvering target tracking," *IEEE Access*, vol. 6, pp. 52544–52560, 2018.

[31] J. Zhao and L. Mili, "A decentralized H-infinity unscented Kalman filter for dynamic state estimation against uncertainties," *IEEE Trans. Smart Grid*, vol. 10, no. 5, pp. 4870–4880, Sep. 2019.

[32] H. Aung, K. Soon Low, and S. Ting Goh, "State-of-charge estimation of lithium-ion battery using square root spherical unscented Kalman filter (Sqrt-UKFST) in nanosatellite," *IEEE Trans. Power Electron.*, vol. 30, no. 9, pp. 4774–4783, Sep. 2015.

[33] X. Liu, H. Qu, J. Zhao, P. Yue, and M. Wang, "Maximum correntropy unscented Kalman filter for spacecraft relative state estimation," *Sensors*, vol. 16, no. 9, p. 1530, Sep. 2016.

[34] D. Meng, L. Miao, H. Shao, and J. Shen, "A seventh-degree cubature Kalman filter," *Asian J. Control*, vol. 20, no. 1, pp. 250–262, Jan. 2018.

[35] Z. Y. Miao, H. Y. Shi, Y. Zhang, and F. Xu, "Neural network-aided variational Bayesian adaptive cubature Kalman filtering for nonlinear state estimation," *Meas. Sci. Technol.*, vol. 28, no. 10, Jul. 2017, Art. no. 105003.

[36] D. M. Blei, A. Kucukelbir, and J. D. McAuliffe, "Variational inference: A review for statisticians," *J. Amer. Stat. Assoc.*, vol. 112, no. 518, pp. 859–877, Jul. 2017.

[37] Y. Huang, Y. Zhang, B. Xu, Z. Wu, and J. A. Chambers, "A new adaptive extended Kalman filter for cooperative localization," *IEEE Trans. Aerosp. Electron. Syst.*, vol. 54, no. 1, pp. 353–368, Feb. 2018.

[38] Y. Huang, Y. Zhang, Z. Wu, N. Li, and J. Chambers, "A novel adaptive Kalman filter with inaccurate process and measurement noise covariance matrices," *IEEE Trans. Autom. Control*, vol. 63, no. 2, pp. 594–601, Feb. 2018.

[39] Y. Y. Huang, Y. W. Jing, and Y.-B. ShI, "Non-parametric mobile node localization for IOT by variational Bayesian approximations adaptive Kalman filter," *Cogn. Syst. Res.*, vol. 52, pp. 27–35, Dec. 2018.

[40] Y. Jiang and V. C. M. Leung, "An asymmetric double sided two-way ranging for crystal offset," in *Proc. Int. Symp. Signals, Syst. Electron.*, Jul. 2007, pp. 525–528.

[41] P. Barsocchi, S. Lenzi, S. Chessa, and G. Giunta, "A novel approach to indoor RSSI localization by automatic calibration of the wireless propagation model," in *Proc. VTC Spring-IEEE 69th Veh. Technol. Conf.*, Apr. 2009, pp. 1–5.

[42] K. C. Ho and L. Yang, "On the use of a calibration emitter for source localization in the presence of sensor position uncertainty," *IEEE Trans. Signal Process.*, vol. 56, no. 12, pp. 5758–5772, Dec. 2008.

[43] K. W. K. Lui, W.-K. Ma, H. C. So, and F. K. W. Chan, "Semi-definite programming algorithms for sensor network node localization with uncertainties in anchor positions and/or propagation speed," *IEEE Trans. Signal Process.*, vol. 57, no. 2, pp. 752–763, Feb. 2009.
[44] M. D. Rahman and K.-B. Yu, "Total least squares approach for frequency estimation using linear prediction," *IEEE Trans. Acoust., Speech, Signal Process.*, vol. 35, no. 10, pp. 1440–1454, Oct. 1987.
[45] A. Sadollah, H. Eskandar, A. Bahreininejad, and J. H. Kim, "Water cycle algorithm with evaporation rate for solving constrained and unconstrained optimization problems," *Appl. Soft Comput.*, vol. 30, pp. 58–71, May 2015.
[46] O. B. Haddad, M. Moravej, and H. A. Loáiciga, "Application of the water cycle algorithm to the optimal operation of reservoir systems," *J. Irrigation Drainage Eng.*, vol. 141, no. 5, May 2015, Art. no. 04014064.
[47] B. Cao, S. Wang, S. Ge, W. Liu, S. Wang, and S. Yi, "Study on the improvement of ultra-wideband localization accuracy in narrow and long space," *Sensor Rev.*, vol. 40, no. 1, pp. 42–53, Nov. 2019.

Bo Cao received the M.S. degree in mechanical design and theory from the China University of Mining and Technology, Xuzhou, China, in 2015, where he is currently pursuing the Ph.D. degree in mechanical design and theory.

He is currently a Lecturer with Anhui Institute of Science and Technology, Bengbu, China. His current research interests include wireless sensor network, ultrawideband (UWB) deployment, improvement positioning accuracy, underground localization and navigation, and machine learning.

Shibo Wang received the Ph.D. degree in mechanical design and theory from the China University of Mining and Technology, Xuzhou, China, in 2007.

He is currently a Professor with the China University of Mining and Technology. His current research interests include tribology, principles of intelligent perception of mining equipment, mechanism of hard rock cutting, and robotic mining technology.

Shirong Ge received the Ph.D. degree in mechanical engineering from the China University of Mining and Technology, Xuzhou, China, in 1989.

He is currently a Professor and the Deputy Secretary of the Party Committee, China University of Mining and Technology, Beijing, China. His research interests include biological tribology, tribology nonlinear theory, disaster relief robot and mining machinery reliability, and other scientific research.

Dr. Ge has won two national second prizes for technological invention and one national second prize for scientific and technological progress. He is currently the Vice-Chairman of the China Coal Society and the Chairman of the China Institute of Mechanical Engineering Friction Branch.

Wanli Liu received the Ph.D. degree from Tianjin University, Tianjin, China, in 2016.

He is currently a Researcher with the Jiangsu Collaborative Innovation Center of Intelligent Mining Equipment, China University of Mining and Technology, Xuzhou, China. His research interests include mobile laser scanning, accuracy improvement light detection and ranging, inertial measurement unit, and underground position and navigation.